Parallel finite-element implementation for higher-order ice-sheet models

Mauro PEREGO, Max GUNZBURGER, John BURKARDT

Department of Scientific Computing, Florida State University, Tallahassee, FL 32306-4120, USA
E-mail: mperego@fsu.edu

ABSTRACT. Higher-order models represent a computationally less expensive alternative to the Stokes model for ice-sheet modeling. In this work, we develop linear and quadratic finite-element methods, implemented on parallel architectures, for the three-dimensional first-order model of Dukowicz and others (2010) that is based on the Blatter–Pattyn model, and for the depth-integrated model of Schoof and Hindmarsh (2010). We then apply our computational models to three of the ISMIP-HOM benchmark test cases (Pattyn and others, 2008). We compare results obtained from our models with those obtained using a reliable Stokes computational model, showing that our first-order model implementation produces reliable and accurate solutions for almost all characteristic length scales of the test geometries considered. Good agreement with the reference Stokes solution is also obtained by our depth-integrated model implementation in fast-sliding regimes and for medium to large length scales. We also provide a comprehensive comparison between results obtained from our first-order model implementation and implementations developed by ISMIP-HOM participants; this study shows that our implementation is at least as good as the previous ones. Finally, a comparison between linear and quadratic finite-element approximations is carried out, showing, as expected, the better accuracy of the quadratic finite-element method.

1. INTRODUCTION

It is widely accepted that ice sheets behave like an incompressible non-Newtonian fluid, modeled by the Stokes equations with nonlinear rheology (Bengtsson, 1994; Gregory and Huybrechts, 2006; Cuffey and Paterson, 2010). Due to the high computational costs associated with the solution of the Stokes equations over large, three-dimensional (3-D) domains, such as Greenland or Antarctica, several approximations have been considered (Hindmarsh, 2004). These approximations exploit the fact that the aspect ratio, δ, between the characteristic thickness and the characteristic horizontal extent of an ice sheet is very small. In increasing order of accuracy of the solution with respect to δ, we have the zeroth-order (ZO) models, such as the shallow-ice approximation (SIA; Hutter, 1983) and the shallow-shelf approximation (Morland, 1987; MacAyeal, 1989), and higher-order models, such as the depth-integrated L1L1 and L1L2 models (Hindmarsh, 2004) and the 3-D Blatter–Pattyn model (Blatter, 1995; Pattyn, 2003), hereafter referred to as the first-order (FO) model.

Higher-order models can be regarded as a trade-off between accuracy and computational costs. In this work, we consider the FO model presented by Dukowicz and others (2010), which is based on the Blatter–Pattyn model (Blatter, 1995; Pattyn, 2003) and the modified version of the L1L2 model of Schoof and Hindmarsh (2010). The resulting mathematical models consist of a system of two nonlinear elliptic equations for the horizontal velocities. The FO model is a fully 3-D model, whereas the L1L2 is depth-integrated and reduces to a two-dimensional (2-D) elliptic system in the horizontal coordinates. Dukowicz and others (2010) and Schoof and Hindmarsh (2010), respectively, show that there exist variational principles associated with both the FO and the L1L2 models. In fact, the two problems are equivalent to the unconstrained minimization of associated positive functionals. In contrast, the Stokes model is equivalent to a constrained minimization problem (Dukowicz and others, 2010) in which the pressure plays the role of a Lagrange multiplier. Therefore, besides the reduction in the number of variables (from four to two), the higher-order models have mathematical properties which are more favorable than the Stokes model from a numerical point of view. Moreover, the L1L2 model has the clear advantage of being a 2-D model.

In this work, we propose a finite-element (FE) approximation of the higher-order models at hand. Using finite elements, complex geometries and unstructured and anisotropic meshes can be naturally handled, as can several physical boundary conditions. Moreover, finite elements are particularly suited for the solution of the problems at hand. In fact, when the bilinear form associated with the weak formulation of the linearized problem is symmetric and coercive, as in the case of the considered higher-order models, Galerkin FE methods become projection methods (Bochev and Gunzburger, 2009). This means that the computed solution is the 'best' approximation to the exact model solution among all possible functions in the chosen FE space.

We implement the higher-order models using the C++ FE library LifeV (www.lifev.org). We compare our implementation against tests A, C and E of the ISMIP-HOM benchmark experiments (Pattyn and others, 2008). In particular, we compare our results with the reference Stokes solutions provided by Gagliardini and Zwinger (2008). We also compare our solutions with those obtained by the higher-order methods presented in the ISMIP-HOM benchmark. It turns out that our FO solutions are in general closer to the reference Stokes solutions than most of the FO solution methods discussed in the ISMIP-HOM benchmark. Also, for medium to small values of the aspect ratio, δ, the proposed L1L2 model presents good agreement with the Stokes solution in the presence of sliding boundary conditions.

In this work, we use both linear (P1) and quadratic (P2) finite elements. Linear elements provide a second-order

accurate approximate solution, whereas quadratic elements provide third-order accuracy (in L^2 norm). A comparison between the solutions obtained with linear and quadratic finite elements is carried out for the FO model. As expected, quadratic elements provide better solutions than linear ones, the improvement being more pronounced in the presence of sliding boundary conditions.

The paper is organized as follows. In section 2, we introduce the FO and L1L2 mathematical models including boundary conditions and weak formulations. A brief derivation of the models as an approximation of the Stokes model is also presented. In section 3, we define the FE discretization of the problems at hand. In section 4, we report on the results of the numerical experiments using three ISMIP-HOM benchmark tests. In particular, we compare our L1L2 and FO models against a Stokes model, compare our FO model to other implementations of the FO model and compare our L1L2 model against other depth-integrated higher-order models. Also we compare the Newton and Picard approaches and the use of structured meshes versus locally refined unstructured meshes. Finally we compare the use of linear and quadratic FE approximations.

2. MATHEMATICAL MODEL

2.1. Stokes model

Ice-sheet flows are typically modeled as non-Newtonian incompressible fluids obeying the Stokes equations. A quasi-static approximation is generally adopted because inertial terms (time derivatives and advective terms) can be neglected, due to the slow movement of the ice. Denoting the ice velocity as **u** and the Cauchy stress tensor as σ, the Stokes model is given by

$$-\nabla \cdot \sigma = \rho \mathbf{g} \qquad \text{and} \qquad \nabla \cdot \mathbf{u} = 0, \qquad (1)$$

where ρ denotes the ice density and **g** the gravitational acceleration, $\mathbf{g} \approx \{0, 0, -|\mathbf{g}|\} = \{0, 0, -g\}$. The Cauchy stress tensor is given by

$$\sigma = \tau - pI = 2\mu\dot{\varepsilon} - pI, \qquad (2)$$

where τ denotes the deviatoric stress tensor, μ the ice effective viscosity, p the ice pressure, I the identity tensor and $\dot{\varepsilon}$ the strain-rate tensor defined as

$$\dot{\varepsilon}_{ij} = \frac{1}{2}\left(\frac{\partial u_i}{\partial x_j} + \frac{\partial u_j}{\partial x_i}\right). \qquad (3)$$

The effective viscosity, μ, is given by Glen's law (Nye, 1957; Cuffey and Paterson, 2010)

$$\mu = \frac{1}{2}A^{-\frac{1}{n}}\dot{\varepsilon}_e^{(\frac{1}{n}-1)} = \frac{1}{2}A^{-1}\tau_e^{1-n}, \qquad (4)$$

where the effective strain rate, $\dot{\varepsilon}_e$, and the effective stress, τ_e, are given by

$$\dot{\varepsilon}_e = \sqrt{\frac{1}{2}\sum_{ij}\dot{\varepsilon}_{ij}^2} \qquad \text{and} \qquad \tau_e = \sqrt{\frac{1}{2}\sum_{ij}\tau_{ij}^2} \qquad (5)$$

and where A denotes the flow rate factor which is strongly dependent on the ice temperature.

Stokes boundary conditions

Let the ice domain, Ω, be bounded by the upper surface, Γ_s, the lower surface, Γ_b, and the vertical lateral surface, Γ_l, defined as

$$\Gamma_s = \{(x, y, z) \mid z = s(x, y)\}, \quad \Gamma_b = \{(x, y, z) \mid z = b(x, y)\},$$
$$\Gamma_l = \{(x, y, z) \mid l(x, y) = 0\}. \qquad (6)$$

We require that $\Gamma_s \cup \Gamma_b \cup \Gamma_l = \partial\Omega$, the whole boundary of Ω. The lateral surface, Γ_l, can be void.

On the upper surface, a *stress-free* boundary condition is prescribed:

$$\sigma\mathbf{n} = \mathbf{0} \quad \text{on } \Gamma_s, \qquad (7)$$

where **n** is the unit vector normal to the surface and outward-pointing. On the lower surface, we consider *no-slip* or *sliding* boundary conditions, i.e. if we partition Γ_b into Γ_0 and Γ_β, we have

$$\begin{cases} \mathbf{u} = \mathbf{0} & \text{on } \Gamma_0 \\ \mathbf{u} \cdot \mathbf{n} = 0 \quad \text{and} \quad (\sigma\mathbf{n} + \beta\,\mathbf{u})_\| = \mathbf{0} & \text{on } \Gamma_\beta, \end{cases} \qquad (8)$$

where $\beta \geq 0$ is the sliding coefficient and the operator $(\cdot)_\|$ performs the tangential projection onto the surface.

2.2. First-order model

The FO model is derived as an approximation of the Stokes model under the assumption that the aspect ratio, δ, is small and that the normals to the upper and lower surfaces are almost in the vertical direction, that is, $\mathbf{n} \sim [O(\delta), O(\delta), 1]^T$. Loosely speaking, the FO model is obtained neglecting those terms of the Stokes model that are $O(\delta^2)$ (Blatter, 1995; Pattyn, 2003; Dukowicz and others, 2010).

We denote with u, v and w the components of the velocity along the x, y and z directions, respectively. In the first-order approximation, the terms $\partial w/\partial x$ and $\partial w/\partial y$ are negligible with respect to $\partial u/\partial z$; hence, $\dot{\varepsilon}_{xz}$ and $\dot{\varepsilon}_{yz}$ are approximated as $\dot{\varepsilon}_{xz} \approx \frac{1}{2}(\partial u/\partial z)$ and $\dot{\varepsilon}_{yz} \approx \frac{1}{2}(\partial v/\partial z)$, respectively. Exploiting the fact that, due to incompressibility, $\dot{\varepsilon}_{zz} = -(\dot{\varepsilon}_{xx} + \dot{\varepsilon}_{yy})$, the effective strain rate reduces to

$$\dot{\varepsilon}_e^2 = \dot{\varepsilon}_{xx}^2 + \dot{\varepsilon}_{yy}^2 + \dot{\varepsilon}_{xx}\dot{\varepsilon}_{yy} + \dot{\varepsilon}_{xy}^2 + \dot{\varepsilon}_{xz}^2 + \dot{\varepsilon}_{yz}^2. \qquad (9)$$

Moreover, the terms $\partial\sigma_{zx}/\partial x$ and $\partial\sigma_{zy}/\partial y$ are negligible with respect to $\partial\sigma_{zz}/\partial z$; therefore from the vertical component of the momentum equation (Equation (1)), we have

$$\frac{\partial}{\partial z}\left(-2\mu\dot{\varepsilon}_{zz} + p\right) = -\rho g. \qquad (10)$$

Integrating this equation along the vertical direction between z and the top surface, s, and prescribing the stress-free boundary condition on that surface, we obtain an expression for the pressure:

$$p = 2\mu\dot{\varepsilon}_{zz} + \rho g(s - z) = -2\mu\left(\dot{\varepsilon}_{xx} + \dot{\varepsilon}_{yy}\right) + \rho g(s - z). \qquad (11)$$

Substituting Equation (11) into the horizontal components of the momentum equation (Equation (1)), we obtain the first-order equations

$$\begin{cases} -\nabla \cdot (2\mu\,\dot{\boldsymbol{\varepsilon}}_1) = -\rho g\dfrac{\partial s}{\partial x} \\ -\nabla \cdot (2\mu\,\dot{\boldsymbol{\varepsilon}}_2) = -\rho g\dfrac{\partial s}{\partial y}, \end{cases} \qquad (12)$$

where

$$\dot{\boldsymbol{\varepsilon}}_1 = \begin{bmatrix} 2\dot{\varepsilon}_{xx} + \dot{\varepsilon}_{yy} \\ \dot{\varepsilon}_{xy} \\ \dot{\varepsilon}_{xz} \end{bmatrix} \quad \text{and} \quad \dot{\boldsymbol{\varepsilon}}_2 = \begin{bmatrix} \dot{\varepsilon}_{yx} \\ \dot{\varepsilon}_{xx} + 2\dot{\varepsilon}_{yy} \\ \dot{\varepsilon}_{yz} \end{bmatrix}.$$

(13)

Boundary conditions for the first-order equations
In the FO approximation, the boundary conditions (Equations (7) and (8)) reduce to

$$
\begin{array}{lll}
\dot{\boldsymbol{\varepsilon}}_1 \cdot \mathbf{n} = 0, & \dot{\boldsymbol{\varepsilon}}_2 \cdot \mathbf{n} = 0 & \text{on } \Gamma_s \\
u = 0, & v = 0 & \text{on } \Gamma_0 \\
2\mu\,\dot{\boldsymbol{\varepsilon}}_1 \cdot \mathbf{n} + \beta u = 0, & 2\mu\,\dot{\boldsymbol{\varepsilon}}_2 \cdot \mathbf{n} + \beta v = 0 & \text{on } \Gamma_\beta.
\end{array}
$$

(14)

These boundary conditions, proposed by Dukowicz and others (2010), are slightly different from those proposed by Pattyn (2003). Pattyn (2003) takes the normals, $\mathbf{n}$, as $\left[-\frac{\partial s}{\partial x}, -\frac{\partial s}{\partial y}, 1 \right]^{\mathrm{T}}$ on Γ_s and $\left[\frac{\partial b}{\partial x}, \frac{\partial b}{\partial y}, -1 \right]^{\mathrm{T}}$ on Γ_β, whereas we normalize them to have unit length, i.e. we divide them by $\sqrt{(\partial s/\partial x)^2 + (\partial s/\partial y)^2 + 1}$ and $\sqrt{(\partial b/\partial x)^2 + (\partial b/\partial y)^2 + 1}$, respectively.

Weak formulation of the first-order equations
We denote with V the Hilbert space defined as $V = \{\varphi \in H^1(\Omega) : \varphi|_{\Gamma_0} = 0\}$. Here, $H^1(\Omega)$ denotes the space of square-integrable functions whose first derivatives are also square integrable. The weak formulation of Equation (12) reads: find $u, v \in V$ such that

$$
\begin{cases}
\displaystyle\int_\Omega 2\mu\,\dot{\boldsymbol{\varepsilon}}_1(u, v) \cdot \nabla\varphi_1 \mathrm{d}\Omega + \int_{\Gamma_\beta} \beta u \varphi_1 \mathrm{d}\Gamma + \int_\Omega \rho g \frac{\partial s}{\partial x} \varphi_1 \mathrm{d}\Omega = 0 \\
\displaystyle\int_\Omega 2\mu\,\dot{\boldsymbol{\varepsilon}}_2(u, v) \cdot \nabla\varphi_2 \mathrm{d}\Omega + \int_{\Gamma_\beta} \beta v \varphi_2 \mathrm{d}\Gamma + \int_\Omega \rho g \frac{\partial s}{\partial y} \varphi_2 \mathrm{d}\Omega = 0
\end{cases}
$$

(15)

for all $\varphi_1, \varphi_2 \in V(\Omega)$. Whenever periodic boundary conditions are applied on Γ_l, we require that the functions in V be periodic. (Salsa, 2008, provides an introduction to Sobolev spaces and weak formulation.)

We define the operator $\mathcal{F}(u, v; \varphi_1, \varphi_2)$ as the left-hand side of the system given in Equation (15).

Then, the problem of Equation (15) is equivalent to finding the root $(u, v) \in [V]^2$ of the nonlinear equation

$$\mathcal{F}(u, v; \varphi_1, \varphi_2) = 0 \qquad \forall (\varphi_1, \varphi_2) \in [V]^2.$$

(16)

In order to find the roots of Equation (16), we use Newton's method. Details are given in the Appendix. Newton's method is an iterative algorithm and requires an initial guess, (u^0, v^0).

It is not possible to take $(0, 0)$ as the initial guess because in this case the effective viscosity, μ, would not be defined. Instead, we compute (u^0, v^0) by solving Equation (15) for a given viscosity, $\widetilde{\mu}$. (The value of $\widetilde{\mu}$ influences the convergence of the iterative scheme. Here we take $\widetilde{\mu} = 0.5 \times 10^8\,\mathrm{Pa\,a\,m^{-1}}$, which has been determined empirically. If an estimate of the effective strain, $\widetilde{\dot{\varepsilon}}_e$, is available, one can take $\widetilde{\mu} = \frac{1}{2}A^{-\frac{1}{n}}\widetilde{\dot{\varepsilon}}_e^{(\frac{1}{n}-1)}$.)

2.3. L1L2 approximation

The L1L2 model approximates the FO model, retaining almost the same order of accuracy. It requires the solution of 2-D nonlinear partial differential equations. The L1L2 model presented here is derived by Schoof and Hindmarsh (2010), where it is shown to have the same accuracy as the FO model for fast-sliding regimes. It is devised for sliding boundary conditions and, in the limit case of no-slip boundary conditions, it reduces to the zeroth-order SIA model. The model proposed by Schoof and Hindmarsh (2010) is limited to planar geometries living in the vertical *x-z* plane. Here we present its natural extension to 3-D geometries.

We define the norm $|\cdot|_\parallel$ as

$$|\dot{\varepsilon}|_\parallel^2 = \dot{\varepsilon}_{xx}^2 + \dot{\varepsilon}_{yy}^2 + \dot{\varepsilon}_{xx}\dot{\varepsilon}_{yy} + \dot{\varepsilon}_{xy}\dot{\varepsilon}_{yx}$$

(17)

and the norm $|\cdot|_\perp$ as

$$|\dot{\varepsilon}|_\perp^2 = \dot{\varepsilon}_{xz}^2 + \dot{\varepsilon}_{yz}^2.$$

(18)

We also denote with $\nabla_\parallel$ the operator $\frac{\partial}{\partial x}\mathbf{i} + \frac{\partial}{\partial y}\mathbf{j}$.

The effective deviatoric stress reads $\tau_e^2 = |\tau|_\parallel^2 + |\tau|_\perp^2$. For the L1L2 model, we use the SIA (Hutter, 1983) to estimate $|\tau|_\perp^2$:

$$|\tilde{\tau}|_\perp^2 = \left[\rho g(s - z)|\nabla_\parallel s|\right]^2.$$

(19)

Hence, we have

$$\tau_e^2 \approx |\tau|_\parallel^2 + |\tilde{\tau}|_\perp^2.$$

(20)

We then approximate the horizontal components of $\dot{\varepsilon}$ at the bedrock ($z = b$) with

$$\dot{\varepsilon}_{ij}\big|_{z=b} = A\left(|\tau|_\parallel^2 + |\tilde{\tau}|_\perp^2\right)^{\frac{n-1}{2}} \tau_{ij} \quad \text{for } i, j \in \{x, y\}.$$

(21)

Taking the norm $|\cdot|_\parallel$ of both sides of Equation (21), we obtain

$$|\dot{\varepsilon}_b|_\parallel = A\left(|\tau|_\parallel^2 + |\tilde{\tau}|_\perp^2\right)^{\frac{n-1}{2}} |\tau|_\parallel,$$

(22)

where $\dot{\varepsilon}_b = \dot{\varepsilon}|_{z=b}$. Equation (22) implicitly defines $|\tau|_\parallel$ as a function of $|\dot{\varepsilon}_b|_\parallel$ and $|\tilde{\tau}|_\perp$. This allows us to solve Equation (21) and determine the horizontal components of τ:

$$\tau_{ij} = A^{-1}\left(|\tau|_\parallel^2 + |\tilde{\tau}|_\perp^2\right)^{\frac{1-n}{2}} \dot{\varepsilon}_{ij}\big|_{z=b} = 2\mu\left(|\dot{\varepsilon}_b|_\parallel, |\tilde{\tau}|_\perp\right) \dot{\varepsilon}_{ij}\big|_{z=b}.$$

(23)

Integrating the first-order equation (12) from $z = b$ to $z = s$, and applying the sliding boundary conditions (Equation (14)$_{1,3}$) we have

$$
\begin{cases}
-\nabla_\parallel \cdot \left(2\bar{\mu}\,\dot{\boldsymbol{\varepsilon}}_{1,b}\right) + \beta u_b = -\rho g H \dfrac{\partial s}{\partial x} \\
-\nabla_\parallel \cdot \left(2\bar{\mu}\,\dot{\boldsymbol{\varepsilon}}_{2,b}\right) + \beta v_b = -\rho g H \dfrac{\partial s}{\partial y},
\end{cases}
$$

(24)

where

$$\bar{\mu}(x, y) = \int_b^s \mu\left(|\dot{\varepsilon}_b|_\parallel, |\tilde{\tau}|_\perp\right) \mathrm{d}z$$

(25)

and

$$\dot{\boldsymbol{\varepsilon}}_1 = \begin{bmatrix} 2\dot{\varepsilon}_{xx} + \dot{\varepsilon}_{yy} \\ \dot{\varepsilon}_{xy} \end{bmatrix} \quad \text{and} \quad \dot{\boldsymbol{\varepsilon}}_2 = \begin{bmatrix} \dot{\varepsilon}_{yx} \\ \dot{\varepsilon}_{xx} + 2\dot{\varepsilon}_{yy} \end{bmatrix}.$$

(26)

Solving these equations we obtain the basal velocities, $u_b(x, y)$ and $v_b(x, y)$.

In order to obtain the velocities, $u(x, y, z)$ and $v(x, y, z)$, we need to compute τ_{xz} and τ_{yz}. Integrating the first-order equation (12), along the vertical direction, from z, and

applying stress-free boundary conditions (Equation (14)$_1$), we have

$$\tau_{xz} = \nabla_\| \cdot \left(2\bar{\mu}_s\,\dot{\boldsymbol{\varepsilon}}_{1,b}\right) - \rho g \frac{\partial s}{\partial x}(s - z)$$

$$\tau_{yz} = \nabla_\| \cdot \left(2\bar{\mu}_s\,\dot{\boldsymbol{\varepsilon}}_{2,b}\right) - \rho g \frac{\partial s}{\partial y}(s - z),$$

(27)

where

$$\bar{\mu}_s = \int_z^s \mu\left(|\dot{\varepsilon}_b|_\|\,,|\tilde{\tau}|_\perp\right) \mathrm{d}z.$$

(28)

The effective stress, τ_e, can be recovered as

$$\tau_e^2 = |\tau|_\|^2 + |\tau|_\perp^2 = 4\mu\left(|\dot{\varepsilon}_b|_\|\,,|\tilde{\tau}|_\perp\right)^2\,|\varepsilon_b|_\|^2 + \tau_{xz}^2 + \tau_{yx}^2.$$ (29)

The horizontal velocity components, u and v, are obtained by integrating $\varepsilon_{iz} = A\tau_e^{n-1}\tau_{iz}$ for $i \in \{x, y\}$

$$u = u_b + 2\int_b^z A\tau_e^{n-1}\tau_{xz}\,\mathrm{d}z, \quad v = v_b + 2\int_b^z A\tau_e^{n-1}\tau_{yz}\,\mathrm{d}z.$$

(30)

Note that Equations (24) are only defined when sliding boundary conditions are prescribed at the bedrock. In the limit case of no-slip boundary conditions, the basal velocity components are known ($u_b = v_b = 0$), and the stress terms, τ_{xz} and τ_{yz}, as well as the velocities, u and v, reduce to the SIA values. In this case, the horizontal velocity components read

$$u = \rho g\, G\,\frac{\partial s}{\partial x}, \qquad v = \rho g\, G\,\frac{\partial s}{\partial y},$$ (31)

with $G = \dfrac{2A}{n+1}\left[(s-z)^{n+1} - H^{n+1}\right]|\rho g \nabla_\| s|^{n-1}$.

Weak formulation of the L1L2 problem
The nonlinear elliptic equations (24) are solved in the 2-D domain, Σ, which is the projection of Ω onto the x-y plane. Typically, stress-free or no-slip boundary conditions are prescribed on $\partial\Sigma$. We denote with $\Lambda_0, \Lambda_s, \Lambda_l$ the portions of $\partial\Sigma$ where no-slip, stress-free and periodic boundary conditions are prescribed, respectively. The weak formulation for Equation (24) is similar to the FO one. We define the Hilbert space, V_Σ, as $V_\Sigma = \{\varphi \in H^1(\Sigma) : \varphi|_{\Lambda_0} = 0\}$. The weak formulation of the problem is given by: find $u, v \in V_\Sigma$ such that

$$\begin{cases} \int_\Sigma \left(2\bar{\mu}\,\dot{\boldsymbol{\varepsilon}}_{1,b}(u,\,v)\cdot\nabla_\|\varphi_1 + \beta u\varphi_1\right)\mathrm{d}\Sigma = -\int_\Sigma \rho g H\frac{\partial s}{\partial x}\varphi_1\mathrm{d}\Sigma \\ \int_\Sigma \left(2\bar{\mu}\,\dot{\boldsymbol{\varepsilon}}_{2,b}(u,\,v)\cdot\nabla_\|\varphi_2 + \beta v\varphi_2\right)\mathrm{d}\Sigma = -\int_\Sigma \rho g H\frac{\partial s}{\partial y}\varphi_2\mathrm{d}\Sigma \end{cases}$$

(32)

for all $\varphi_1,\,\varphi_2 \in V_\Sigma$. When periodic boundary conditions are applied on Λ_l, we require that the functions in V_Σ be periodic, while stress-free boundary conditions (on Λ_s) are naturally included in the weak formulation. As in the FO case, we use Newton's method to solve the problem. Details are given in the Appendix.

3. NUMERICAL DISCRETIZATION AND IMPLEMENTATION

In this section we briefly describe the FE discretization of the weak formulation, Equation (15). (See, e.g., Quarteroni and Valli, 1994; Quarteroni, 2009, for an introduction to FE methods.) The discretization for the 2-D case, i.e. for the

formulation of Equation (32), is not provided here because it can be inferred from the 3-D one. In particular, a triangular mesh is considered instead of a tetrahedral one.

Let $\mathcal{T}_h$ denote a tetrahedral triangulation of the ice domain, Ω. Here, h is the maximum diameter of the tetrahedral elements in $\mathcal{T}_h$. We consider the FE space $P_{k,h}(\mathcal{T}_h)$ consisting of continuous functions on Ω whose restriction to any tetrahedron in $\mathcal{T}_h$ is a polynomial of degree k. We denote with P1 and P2 the FE space associated with $P_{1,h}$ and $P_{2,h}$, respectively. The four (three in 2-D) degrees of freedom (DOF) of P1 elements correspond to values at the vertices of the tetrahedra (triangles in 2-D). The ten (six in 2-D) DOF of P2 elements correspond to values at the vertices of the tetrahedra and at the midpoints of the edges of the tetrahedra (triangles in 2-D). We denote with V_h the finite-dimensional subspace of V defined as $V_h = \{v_h \in P_{k,h} : v_h|_{\Gamma_0} = 0\}$ for $k = 1$ or 2, depending on the finite element chosen. The discretized problem follows from the continuous weak formulation, Equation (15), by replacing V with V_h.

Numerical implementation
The numerical model has been implemented using the C++ parallel FE library 'LifeV', which interfaces with 'Trilinos' (http://trilinos.sandia.gov) for parallel solvers and data structures. The discrete operators are assembled using different quadrature rules. When using P1 elements, we used a 1-point quadrature rule for assembling the stiffness matrix because in this case the gradients of the basis functions are constant on each element. We used a 15-point (6-point in 2-D), fourth-order accurate quadrature rule in the P2 case. The meshes are partitioned using 'Parmetis' (http://glaros.dtc.umn.edu/gkhome/metis/parmetis/overview). The Trilinos package 'NOX' is used to solve the nonlinear system with Newton's method. When the convergence of Newton's method is not monotonic, the solver uses a backtrack algorithm which halves the Newton increment, (δ_u^{k+1}, δ_v^{k+1}), until the infinity norm of $\mathcal{F}^{k+1}$ is less than that of $\mathcal{F}^k$. The stopping criterion is on the l^2 norm of $\mathcal{F}^{k+1}$. The tolerance tol $= 1 \times 10^{-5}$ is used. An average of 6 iterations were needed to reach convergence for tests A and C, whereas up to 14 iterations were needed for test E. The initial guess, (u^0, v^0), is computed solving the first-order equations with the constant viscosity $\tilde{\mu} = 0.5 \times 10^8\,\mathrm{Pa\,a\,m}^{-1}$.

The inner linear Jacobian system is solved with GMRES, preconditioned with the Schwarz method. More precisely the global preconditioner, P_g, is defined as $P_g^{-1} = \sum_{i=1}^N R^\mathsf{T} P_i^{-1} R$, where N is the number of processors, P_i is the preconditioner at the local (processor) level and R is a restriction matrix that extracts local DOF out of the global ones. Unless otherwise specified, the local preconditioner, P_i, is chosen to be the KLU factorization of the restriction of the system matrix belonging to each processor, which means that at the processor level the system is directly solved. GMRES and KLU are implemented in the Trilinos packages 'Belos' and 'Ifpack', respectively. The tolerance tol $= 1 \times 10^{-6}$ was used for the GMRES method. Most of the problems are solved without overlap, but we had to use one row of overlap among the processors to achieve convergence for tests A and C with $L = 5$ km (see section 4). We emphasize that computational efficiency is not a goal of this paper; therefore, the choices made for solvers and preconditioners are likely to be far from optimal.
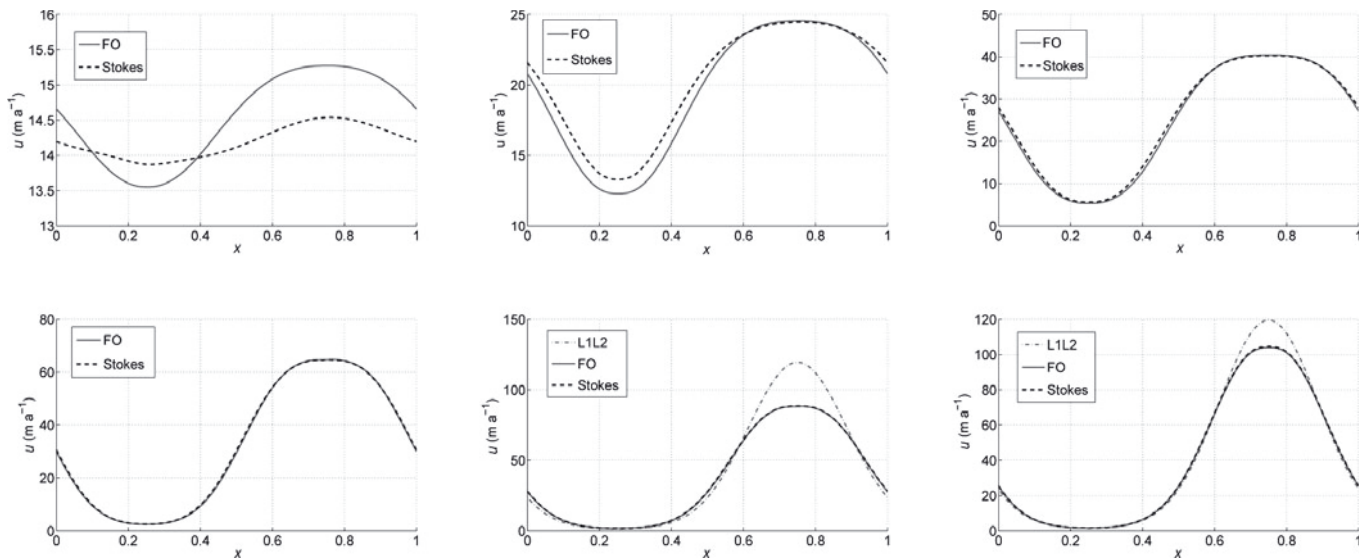
Fig. 1. Test A. For each length, L, the surface velocity component, u, as a function of x, at $y = L/4$. (Dash-dotted curve: our L1L2 solution. Solid curve: our FO solution. Dashed curve: reference Stokes solution.) From left to right, from top to bottom, $L = 5$, 10, 20, 40, 80 and 160 km.

4. NUMERICAL COMPARISONS USING THE ISMIP-HOM BENCHMARK

We consider tests A, C and E described in the ISMIP-HOM benchmark. In the following, we compare our solutions against those obtained by the 'oga' group (Gagliardini and Zwinger, 2008) participating in ISMIP-HOM. The numerical results of the participants in the benchmarking can be downloaded from http://homepages.ulb.ac.be/~fpattyn/ismip/. The physical parameters used in all the experiments are given in Table 1.

The geometry of tests A and C is a horizontal periodic domain with a square unit cell of length L. The bedrock surface, Γ_b, is given by $z = b(x, y)$ and the top surface, Γ_s, by $z = s(x, y)$. In both the tests, the geometry is a regular mapping of a cube. We construct a structured mesh of a unit cube, consisting of $n_x \times n_y \times n_z$ sub-cubes. Each sub-cube is divided into two right prisms with triangular bases that are parallel to the x-y plane. In turn, each prism is then divided into three tetrahedra. The cube is then mapped into the geometry of the test cases by applying the transformation

$$x = LX, \qquad y = LY, \qquad z = s(x, y)Z + b(x, y)(1 - Z), \quad (33)$$

where X, Y, Z are the coordinates of the unit cube and the length, L, and functions b and s are specified in each test. In the case of the L1L2 method, the geometry reduces to a square, divided into $n_x \times n_y$ sub-squares which, in turn, are split into two triangles.

4.1. Test A: comparison of the FO and L1L2 models with the Stokes model

The bedrock and top surfaces (km) are characterized by

$$s(x, y) = -x \tan(\alpha)$$
$$b(x, y) = s(x, y) - 1 + 0.5 \sin\left(\frac{2\pi}{L}x\right) \sin\left(\frac{2\pi}{L}y\right) \quad (34)$$

with $\alpha = 0.5°$. The no-slip boundary condition is prescribed on Γ_b ($\Gamma_0 \equiv \Gamma_b$ and $\Gamma_\beta = \emptyset$), stress-free boundary conditions are prescribed on the top surface and periodic boundary conditions horizontally (on Γ_l). Different domain sizes are

considered; namely we consider $L = 5$, 10, 20, 40, 80 and 160 km.

The results shown are obtained with P2 elements on a $40 \times 40 \times 10$ mesh for the FO model and on a 40×40 mesh for the L1L2 model. The velocity component, u, at the upper surface plotted as a function of x for $y = L/4$ is shown in Figure 1. Our FO solution (solid curve) and the reference Stokes solution (dashed curve) are reported. The L1L2 (SIA) solution is the same for all the length scales (after normalization), therefore, for the sake of visualization, it is reported (dash-dotted curve) only for $L = 80$ and 160 km. The SIA solution is clearly not accurate for $L < 160$ km. We observe, instead, very good agreement in the FO solution for $L \geq 20$ km. As expected, the differences between the FO and Stokes model increase as the aspect ratio increases ($L = 5$ km, $L = 10$ km). In particular, for $L = 5$ km, $\delta \approx 0.2$ and, more importantly, the maximum deviation of the bedrock normal from the z-axis is ~32.5°, which is clearly not negligible. In Figure 2, the shear stress, τ_{xz}, at the bedrock surface is plotted as a function of x for $y = L/4$. Our FO solution (solid curve), L1L2 solution (dash-dotted curve) and the reference Stokes solution (dashed curve) are reported. The same observations as noted for Figure 1 also hold in this case.
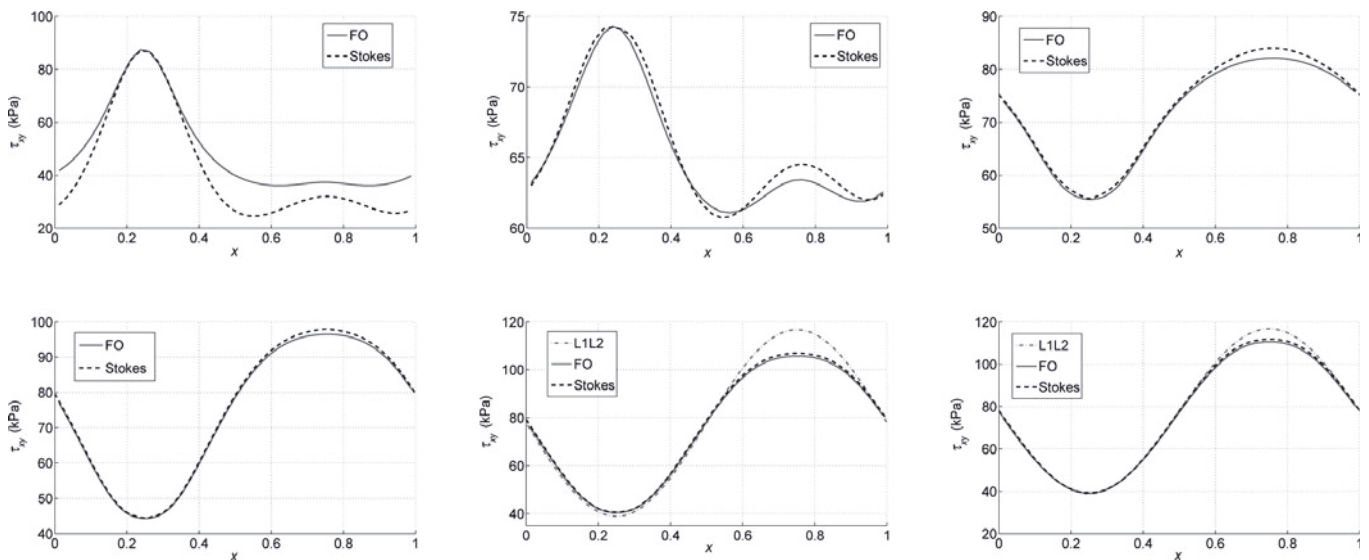
4.2. Test C: comparison of the FO and L1L2 models with the Stokes model

The bedrock and top surfaces (km) are characterized by

$$s(x, y) = -x \tan(\alpha), \qquad b(x, y) = s(x, y) - 1, \quad (35)$$

Table 1. Physical parameters used in the numerical experiments

Symbol	Value	Unit	Description
A	10^{-16}	$Pa^{-n} a^{-1}$	Flow rate factor
n	3		Glen's flow law exponent
g	9.8	$m s^{-2}$	Gravitational constant
ρ	910	$kg m^{-3}$	Ice density

Fig. 2. Test A. For each length, L, the shear stress, τ_{xz}, at the bed as a function of x, at $y = L/4$. (Dash-dotted curve: our L1L2 solution. Solid curve: our FO solution. Dashed curve: reference Stokes solution.) From left to right, from top to bottom, $L = 5$, 10, 20, 40, 80 and 160 km.

with $\alpha = 0.1°$. Sliding boundary conditions are prescribed on the bedrock ($\Gamma_\beta \equiv \Gamma_b$ and $\Gamma_0 = \emptyset$) with β (kPa a m^{-1}) defined as

$$\beta(x, y) = 1 + \sin\left(\frac{2\pi}{L}x\right)\sin\left(\frac{2\pi}{L}y\right). \qquad (36)$$

As before, stress-free boundary conditions are prescribed on the top surface and periodic boundary conditions horizontally. We consider the following values for the domain length: $L = 5$, 10, 20, 40, 80 and 160 km. As for test A, we use P2 elements on a $40{\times}40{\times}10$ mesh for the FO model and on a $40{\times}40$ mesh for the L1L2 model. The velocity component, u, at the upper surface plotted as a function of x for $y = L/4$ is shown in Figure 3. We plot the L1L2 solution (dash-dotted curve), the FO solution (solid curve) and the reference Stokes velocity (dashed curve). We observe good agreement between the L1L2 solution and the Stokes solution for $L \geq 40$ and good agreement between

the FO solution and the Stokes solution for all length scales. Similar results for the shear stress, τ_{xy}, are shown in Figure 4. We observe a remarkable agreement between the FO and Stokes solutions and good agreement between the L1L2 and Stokes solutions. In fact, even for small L, the FO solutions are quite good, which is in contrast with what is observed for test A. However, it should be noted that the slope of the bedrock surface is typically smaller than that of test A. Also, for test C, the bedrock surface is planar, whereas for test A it is a sinusoidal function.

4.3. Test C: comparison of computational costs for the FO and L1L2 models using Newton and Picard methods

Here we compare the CPU times consumed for solving the FO and L1L2 models and using Newton and Picard methods. The Picard method consists of solving Equation (15) or (32), using the viscosity, $\mu = \mu^k$, to obtain a new solution,
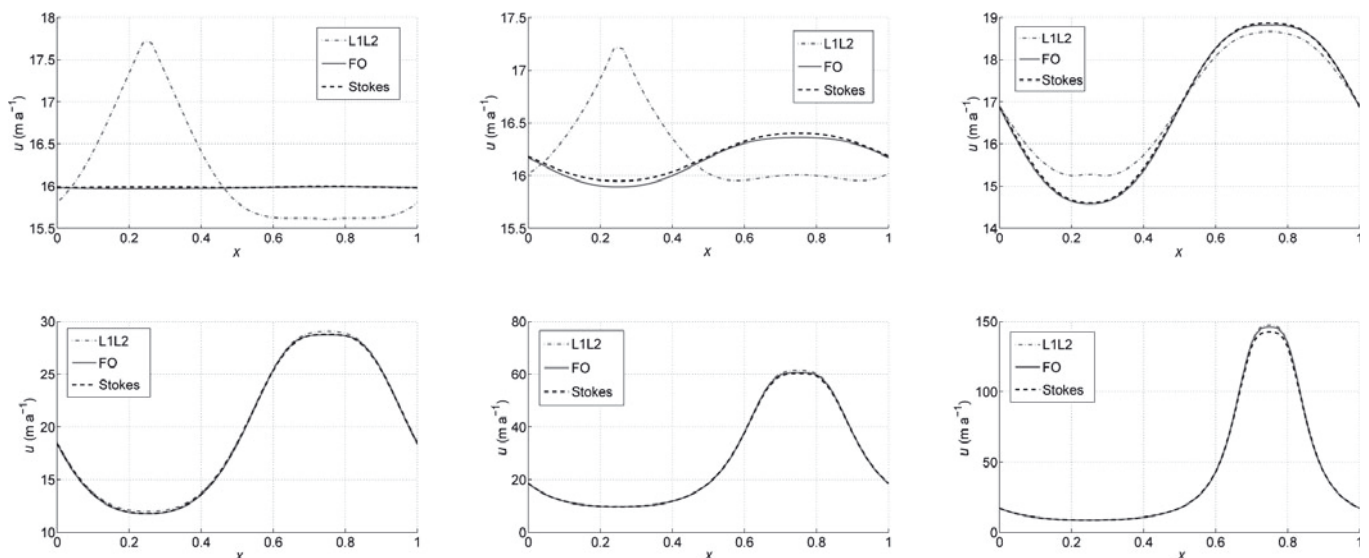
Fig. 3. Test C. For each length, L, the surface velocity component, u, as a function of x, at $y = L/4$. (Dash-dotted curve: our L1L2 solution. Solid curve: our FO solution. Dashed curve: reference Stokes solution.) From left to right, from top to bottom, $L = 5$, 10, 20, 40, 80 and 160 km.
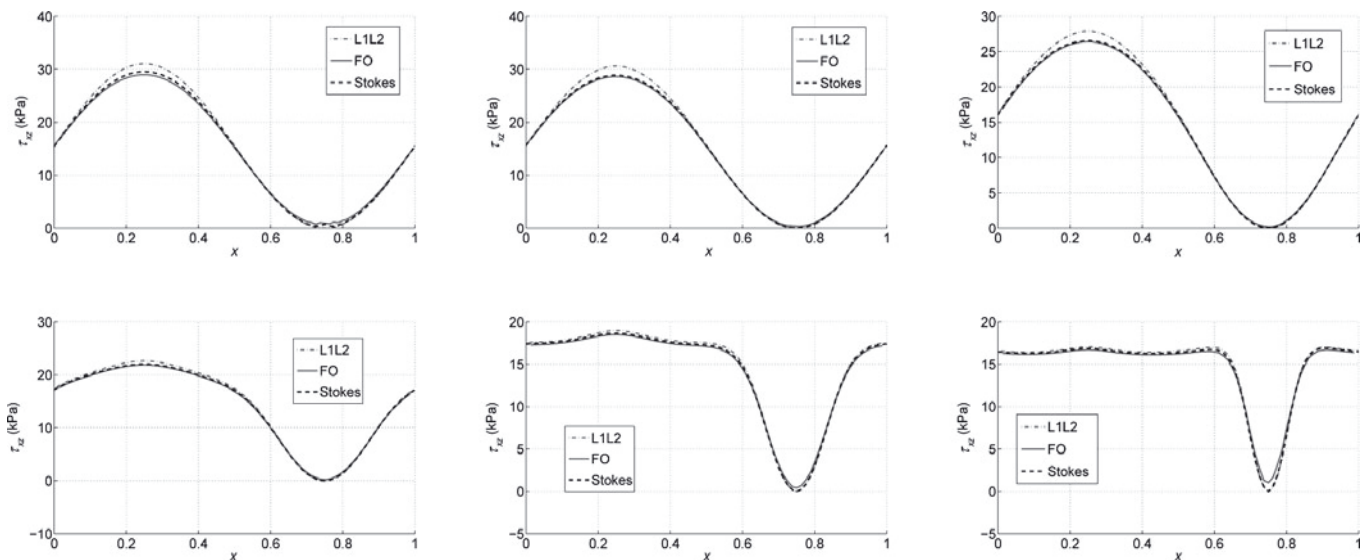
Fig. 4. Test C. For each length, L, the shear stress, τ_{xz}, at the bed as a function of x, at $y = L/4$. (Dash-dotted curve: our L1L2 solution. Solid curve: our FO solution. Dashed line: reference Stokes solution.) From left to right, from top to bottom, $L = 5$, 10, 20, 40, 80 and 160 km.

(u^{k+1}, v^{k+1}). We limit ourselves here to the serial case (a future paper will give a detailed analysis of the performance and scalability of numerical implementations). We use linear FE (P1) and solve test C for $L = 40$ km. The linear systems are solved using GMRES preconditioned with ILU (incomplete LU factorization). Tables 2 and 3 report results for the FO and L1L2 models, respectively. The two tables report the CPU time consumed, the number of nonlinear iterations and the residual depending on the nonlinear solver (Newton or Picard). Two meshes are considered for both the FO and L1L2 models. We used the same discretization steps for the FO and L1L2 models. In particular, for the L1L2 model, the integrals in the z direction are performed using the composite trapezoidal formula with sub-intervals equal, in number, to the vertical layers of the corresponding 3-D mesh. As expected, the L1L2 model is computationally much cheaper than the FO models. Moreover, the Newton method performs better than the Picard method, both in terms of number of iterations and computational costs.

4.4. Test E: comparison of the FO and L1L2 models with the Stokes model

Test E is a 2-D problem in the x-z plane. The geometry is based on data from Haut Glacier d'Arolla, Switzerland; it has a horizontal extension of 5 km, shown in Figure 5. In order to reproduce a 2-D test with 3-D code, we take one layer of elements along the y direction and prescribe periodic boundary conditions on the artificial lateral surfaces. Two boundary conditions are considered. In the first case,

no-slip boundary conditions are prescribed on the bedrock surface ($\Gamma_0 \equiv \Gamma_b$). In the second case, we prescribe sliding boundary conditions, with $\beta = 0$ on the portion Γ_β of the bedrock surface while on the remaining part (Γ_0), no-slip conditions are prescribed; we set $\Gamma_\beta = \{(x, z) \in \Gamma_b, \quad 2.2 \leq x \leq 2.5 \text{ km}\}$. As before, stress-free boundary conditions are prescribed on the top surface.

We first consider the FO model. The results shown are obtained with P2 elements on a $200 \times 1 \times 14$ mesh. The horizontal velocity component, u, is reported in Figure 5. A one-dimensional plot of the surface velocity, u, as a function of x is shown in Figure 6 for the no-slip (left) and sliding (right) cases. Both the FO solution (solid curve) and the Stokes solution (dashed curve) are reported. In this case, the bedrock has large slopes, hence the approximation hypotheses do not hold. However, we still have good agreement between the FO and Stokes solutions.

Similar plots for the shear stress, τ_{xz}, are shown in Figure 7. In the presence of sliding (right), the differences with the Stokes model are notable. However, it is worth mentioning that in the partial-sliding case, even the Stokes shear stress solutions included in the ISMIP-HOM benchmark were rather different from each other. This fact is clear from Figure 8, which shows the surface velocities (left) and basal shear stresses (right) computed by the Stokes models presented in the ISMIP-HOM benchmark. It can be seen that there is also a large variation in the velocity solutions. However, there are three FE models, namely 'oga1', 'aas1' and 'mmr1', which produce the same solution (up to a small tolerance). Moreover, the same Stokes velocity solution is reported in a recently submitted paper by Leng and others

Table 2. Test C, FO. Number of iterations of the nonlinear solver (Newton/Picard), CPU time and Newton/Picard residual. The nonlinear iterations are stopped when the residual is lower than $1 \times 10^{-4} \text{ kPa km}^2$

	Mesh	
	20×20×5 (5292 DOF)	40×40×10 (36 982 DOF)
Iterations	5 / 32	5 / 32
CPU time (s)	10.4/58.6	99/528
Residual	$5.1 \times 10^{-10}/9.7 \times 10^{-5}$	$4.6 \times 10^{-10}/8.5 \times 10^{-5}$

Table 3. Test C, L1L2. Same quantities are reported as for Table 2

	Mesh	
	20×20(×5) (882 DOF)	40×40(×10) (3362 DOF)
Iterations	5/25	7/24
CPU time (s)	0.46/2.10	2.57/10.3
Residual	$1.4 \times 10^{-7}/5.6 \times 10^{-5}$	$1.6 \times 10^{-7}/8.8 \times 10^{-5}$
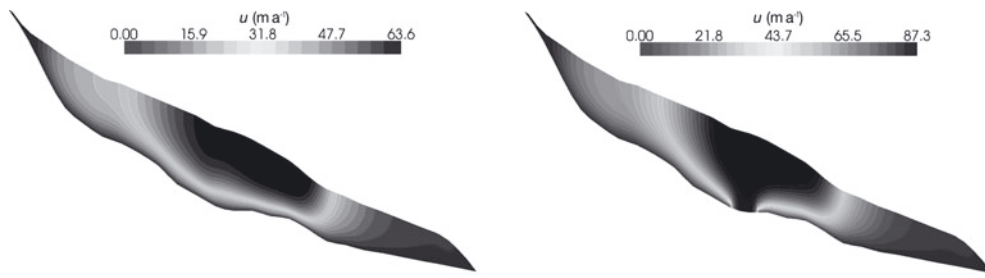
Fig. 5. Test E, FO model. The velocity component, u, on the x-z plane. The plot has been stretched by a factor 4 in the z direction for the sake of visualization. Left: no-slip. Right: partial sliding.
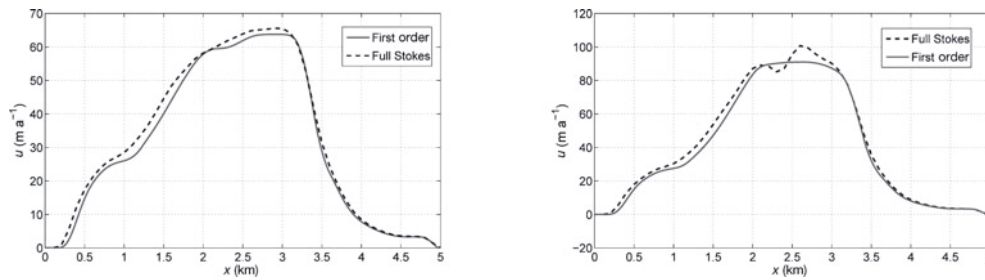
Fig. 6. Test E, FO model. The velocity component, u, on the surface as a function of x. (Dashed curve: reference Stokes solution. Solid curve: our FO solution.) Left: no-slip. Right: partial sliding.
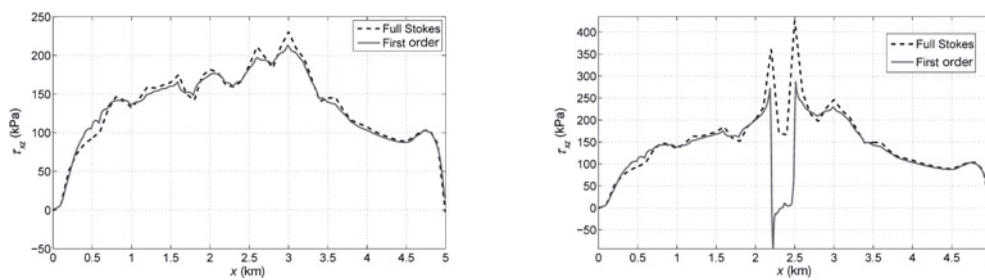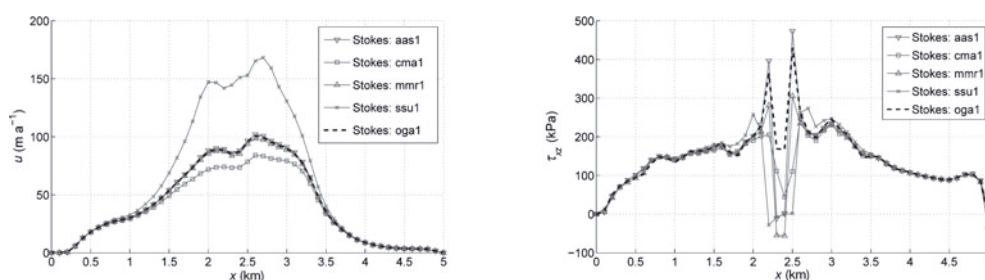

Fig. 7. Test E, FO model. The shear stress, τ_{xz}, on the bed as a function of x. Left: no-slip. Right: partial sliding.

(personal communication from Lili Ju, 2011). Therefore, we believe that, even in the partial-sliding case, the surface velocity solution provided by the 'oga' group is reliable and it is reasonable to compare our model against it.

We next consider the L1L2 model approximation. The velocity component, u, at the surface and shear stress, τ_{xz}, are reported in Figures 9 and 10, respectively. The reference Stokes solution is also reported. It is clear from these figures that the L1L2 model proposed is not adequate to solve test E. This could be partly expected since the

problem features quite large aspect ratio and slope. We note that the shear stress, τ_{xz}, at the bedrock has reasonable agreement with the Stokes solution, while the surface velocity is totally wrong. This could be due to the fact that in slow-sliding regimes, the L1L2 model cannot properly solve the boundary layer close to the free surface (see Schoof and Hindmarsh, 2010). Moreover, in the partial-sliding case, the fast transition between slow- and fast-sliding regimes is difficult to account for by approximations of the Stokes model.
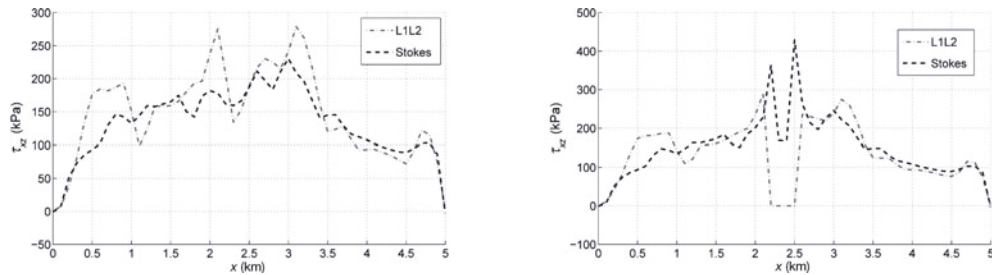

Fig. 8. Test E. Comparison between different Stokes solutions in the partial-sliding case. Left: the velocity component, u, on the surface. Right: the shear stress, τ_{xz}, on the bed.
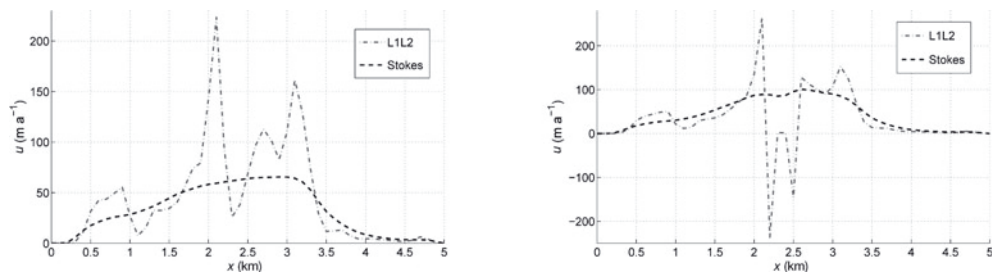
Fig. 9. Test E, L1L2 model. The velocity component, u, on the surface as a function of x. (Dash-dotted curve: L1L2 solution. Dashed curve: reference Stokes solution.) Left: no-slip. Right: partial sliding.

Fig. 10. Test E, L1L2 model. The shear stress, τ_{xz}, on the bed as a function of x. Left: no-slip. Right: partial sliding.

4.5. Test E: comparison between structured grids and a locally refined unstructured grid

Here we stress the fact that finite elements naturally handle nonuniform, unstructured grids. In order to show the potential of this feature, we compare the solutions computed with structured grids and an unstructured grid (Fig. 11, top left) which is refined in proximity to that part of the bedrock where free-slip boundary conditions are prescribed (partial-sliding case). The coarse-structure grid (Fig. 11, bottom left) has about the same number of nodes as the unstructured grid; precisely, the unstructured grid has 428 nodes while the structured grid has 394 nodes. However, the solution computed on the unstructured mesh is much more accurate than that computed with the coarse-structured mesh, and it is almost superimposed on the solution computed with the fine-structured grid (2978 nodes).

4.6. Comparison between different first-order models

Here we compare our FO solutions with the solutions obtained using the FO approximation of the authors of the ISMIP-HOM paper (Pattyn and others, 2008). Some of the ISMIP-HOM participants did not compute all the tests. Most of the FO models presented in the ISMIP-HOM were implemented using finite-difference methods, with the following exceptions: group 'rhi' uses spectral elements, while groups 'cma' and 'bds' use finite elements. We compare the models by looking at the usual plot of the velocity component, u, at the surface as a function of x for $y = L/4$ for test A (Fig. 12), test C (Fig. 13) and test E (Fig. 14). Unfortunately, the 'rhi' group did not perform test E.

In the cases of tests A and C, we considered only the extremal lengths $L = 5$ and 160 km. On the 5 km geometry, test A (Fig. 12, left), no FO solution is close to the Stokes one. However, the 'tpa1' and 'fpa1' solutions are distinguished by being particularly far from it. The same phenomenon is present in test C (Fig. 13, left), where the 'tpa1' and 'fpa1'
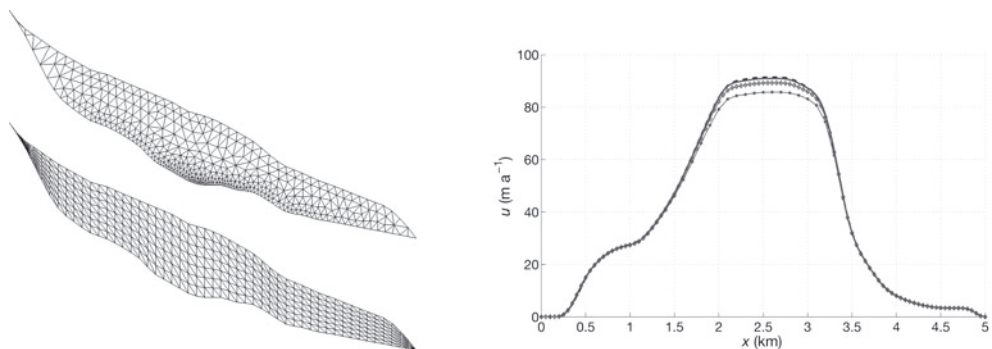
Fig. 11. Test E, partial-sliding case. Left: unstructured mesh (top) and coarse-structured mesh (bottom). Right: the velocity component, u, on the surface as a function of x, computed with FO model and P2 finite elements on different grids. (Dashed curve: unstructured mesh. Solid curve: fine-structured mesh ($200 \times 1 \times 14$). Curve with diamonds: medium-structured mesh ($100 \times 1 \times 10$). Curve with asterisks: coarse-structured mesh ($50 \times 1 \times 7$).)
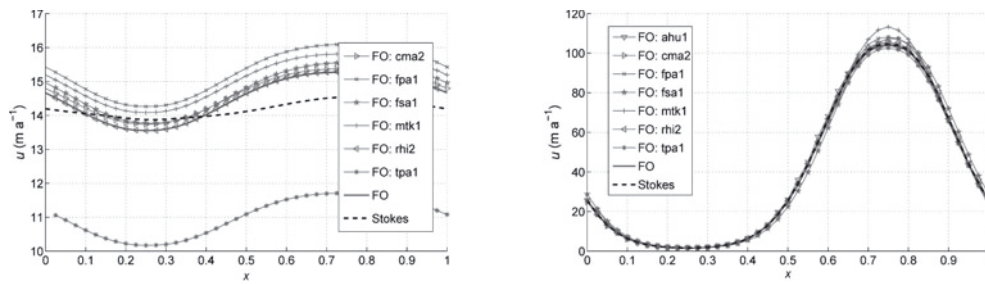
Fig. 12. Test A. Comparison between our FO solution, the reference Stokes solution and the ISMIP-HOM FO models. The upper surface velocity component, u, is plotted as a function of x at $y = L/4$ for the two extremal lengths $L = 5$ km (left) and $L = 160$ km (right).
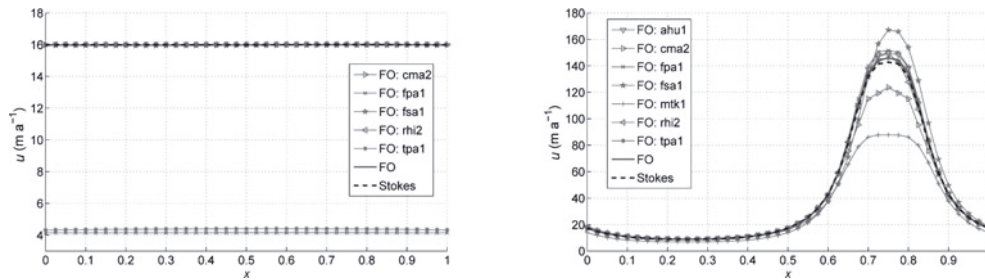
Fig. 13. Test C. Same quantities are plotted as for Figure 12.

solutions are completely wrong, while the remaining models are quite close to the Stokes solution. For $L = 160$ km, test C (Fig. 13, right), we can see that most of the FO models are close to the Stokes solution with the exception of the 'mtk1', 'cma2' and 'fsa1' solutions. The 'rhi2' model and our model are the only ones that show good accuracy in both test A and test C on every length scale.

For test E (Fig. 14), most of the models give accurate solutions in the no-slip case. However, in the partial-sliding case a large variation in the solutions is registered. In this case, the only two FO solutions that are close to the Stokes solution are the 'fpa1' solution and our solution.

### 4.7. Comparison between different depth-integrated higher-order models

Here we compare the proposed L1L2 model with the depth-integrated higher-order models of the authors of the ISMIP-HOM paper (Pattyn and others, 2008). Namely, we compare it with the L1L1 and L1L2 models of group 'rhi' that are based on the work of Hindmarsh (2004) and solved with spectral elements, the L1L2 model by group 'dpo' (Pollard and Deconto, 2007) solved with finite differences and the L1L1 model by group 'lpe' based on MacAyeal (1989) and

Pattyn (2003) and solved with finite differences. Because our L1L2 method is devised for sliding boundary conditions, we only consider Test C. As before, we compare the models by plotting the velocity component, u, at the surface as a function of x for $y = L/4$. Figure 15 shows that our proposed L1L2 model performs well when compared with other higher-order models, for $L \leq 40$. For $L = 5$, only the L1L1 and L1L2 models of group 'rhi' have good agreement with the reference solution, while our model presents a spurious bump in the solution.

4.8. Comparison between linear and quadratic approximations

Here we compare the FE solutions of the FO model obtained using different finite elements (P1 and P2) and different mesh sizes. We first consider test C (Fig. 16), for $L = 5$ km (left) and $L = 160$ km (right). The coarse mesh consists of $20 \times 20 \times 5$ sub-cubes, for a total of 12 000 tetrahedra and 2624 vertices, whereas the fine mesh consists of $60 \times 60 \times 15$ sub-cubes, for a total of 324 000 tetrahedra and 59 536 vertices. When using P1 elements, we have 5292 DOF for the coarse mesh and 119 072 DOF for the fine mesh. Using P2 elements, we
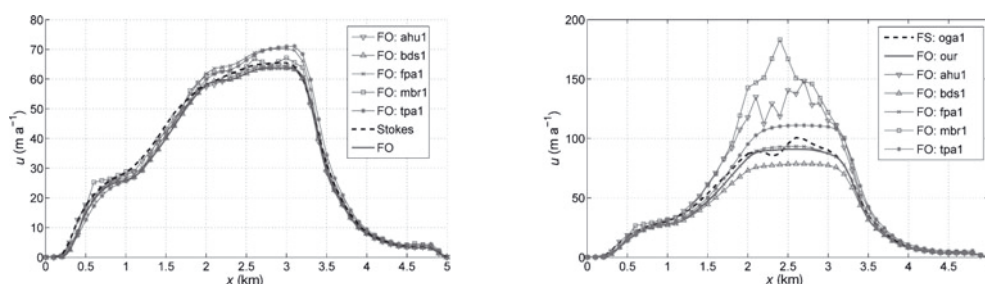
Fig. 14. Test E. Comparison between our FO solution, the reference Stokes solution and those of the ISMIP-HOM FO models. The upper surface velocity component, u, is plotted as a function of x, at $y = L/4$ in the no-slip case (left) and in the partial-sliding case (right).
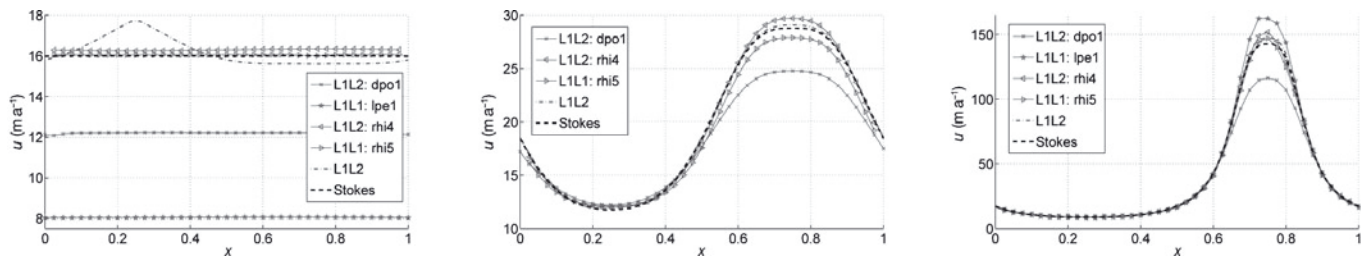
Fig. 15. Test C. Comparison between our L1L2 solution (dash-dotted curve), the reference Stokes solution (dashed curve) and the L1L1, L1L2 models presented in the ISMIP-HOM benchmark. The upper surface velocity component, u, is plotted as a function of x at $y = L/4$ for different length scales. From left to right $L = 5$, 40 and 160 km.

have 36 982 DOF for the coarse mesh, and 907 742 DOF for the fine mesh.

The upper surface velocity (Fig. 16, top) and shear stress, τ_{xz}, on the bed (Fig. 16, bottom) are reported as a function of x at $y = L/4$. The velocity solutions are quite close to one another, even if the differences between the solutions are clear when the velocity scale is enlarged (Fig. 16, top left). Solutions on the coarse grid with P2 elements are comparable to those obtained with P1 elements on the fine mesh, but with one-third the number of DOF. Similar comparisons can be made for the shear stress. In the case $L = 160$ km, the peak of the P2 shear stress on the coarse grid is lower than the correct one; however the overall P2 solution on the coarse grid is comparable with the P1 solution on the fine grid. We consider now test E (Fig. 17). We solve the problem on the coarse mesh, $50 \times 1 \times 7$, and the fine mesh, $200 \times 1 \times 14$. Remarkable differences between the solutions appear in the partial-sliding case (Fig. 17, right). Again, the solution computed with P2 elements on the coarse grid is comparable with the P1 solution on the fine grid.

5. CONCLUDING REMARKS

In this paper we have presented a parallel FE implementation of the FO model (Blatter, 1995; Pattyn, 2003; Dukowicz and others, 2010) and of the L1L2 model (Hindmarsh, 2004; Schoof and Hindmarsh, 2010). We used three of the ISMIP-HOM tests to compare our results against a Stokes model. We showed that, in the case of the FO model, our solutions are very close to the Stokes solutions, except when the geometry featured large variations within a few kilometers (e.g. test A with $L = 5$, 10 km). Good agreement with the Stokes solution occurred also when performing the glacier test case, where the FO hypotheses (low aspect ratio, δ, and small slope) are only partially fulfilled. In the comparison with other FO models participating in ISMIP-HOM benchmarks, we find our FO model provides accurate results in the presence of sliding boundary conditions, whereas most of the others failed in at least one of tests C or E (section 4.6). The L1L2 model features good accuracy properties, again compared with other higher-order models, in the sliding case (test C) for $L \geq 40$ km. However, the solutions can be very inaccurate for large aspect ratios and in the presence of no-slip boundary conditions (in this case the L1L2 model reduces to the zeroth-order SIA model). Overall, the FO model showed itself to be more reliable than the L1L2 model, while the latter has the obvious advantage of being computationally much cheaper.

Our model features both linear and quadratic finite elements. As expected, P2 elements produce more accurate solutions than P1 elements, in particular in the presence
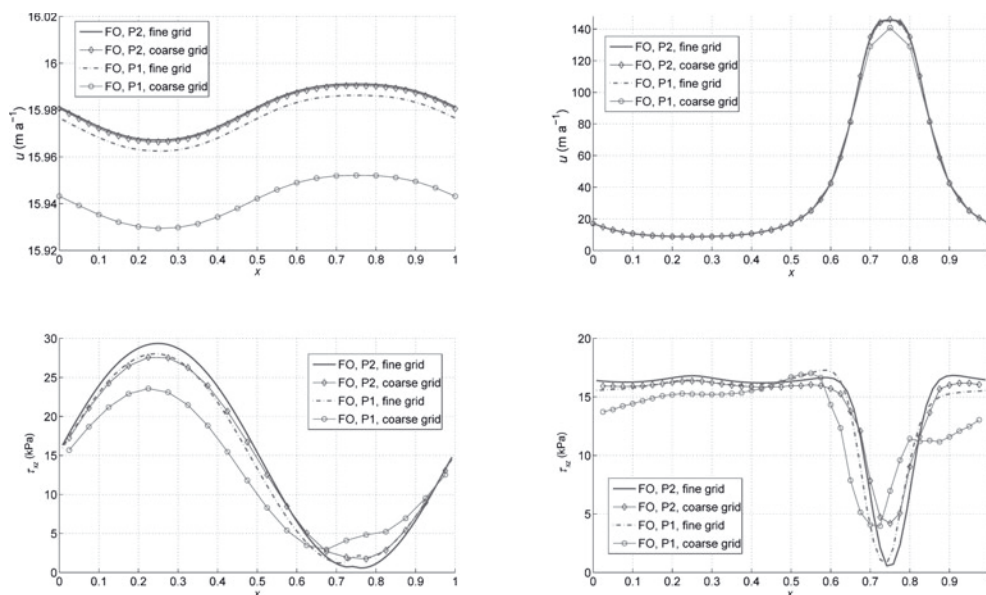
Fig. 16. Test C. Comparison between solutions obtained using different finite elements (P1 and P2) and different meshes ($40 \times 40 \times 10$ and $60 \times 60 \times 15$). Surface velocity component, u (top), and shear stress, τ_{xz}, on the bed (bottom), as a function of x at $y = L/4$, for $L = 5$ km (left) and $L = 160$ km (right).
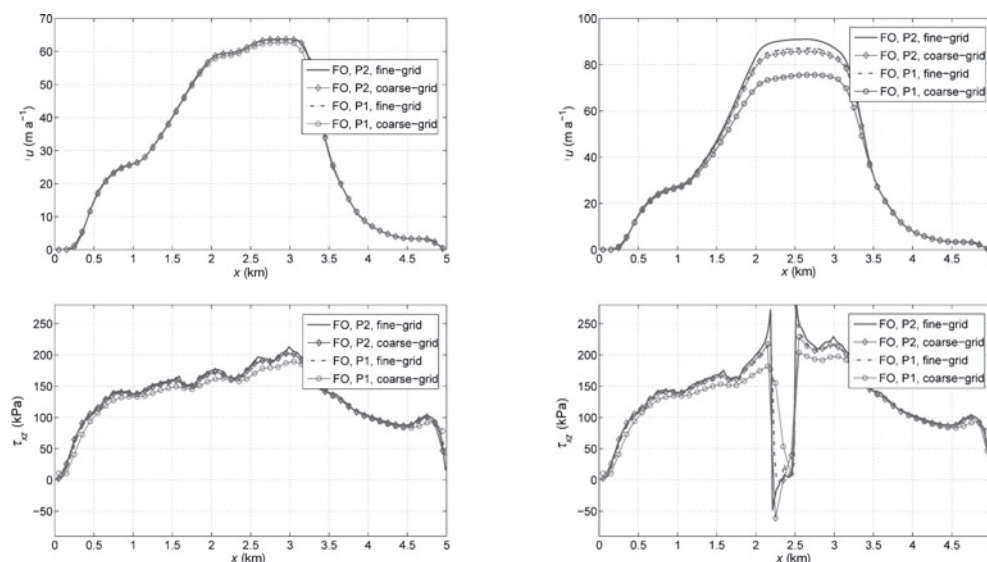
Fig. 17. Test E. Comparison between solutions obtained using different finite elements (P1 and P2) and different meshes ($50 \times 1 \times 7$ or $200 \times 1 \times 14$). Top: velocity component, u, on the surface. Bottom: shear stress, τ_{xz}. Left: no-slip. Right: partial-sliding.

of large variations in the solution. This property can be exploited using coarser grids than those needed when using P1 elements. However, P1 elements feature fewer degrees of freedom, sparser matrices and do not need higher-order quadrature rules. Therefore, a comparison of the computational costs when using P1 and P2 elements is of paramount importance and will be addressed in a forthcoming paper.

Future work will consist of investigating the behavior of both our L1L2 and FO higher-order models and the use of linear and quadratic finite elements on real geometries such as Greenland or Antarctica. The use of more realistic boundary conditions as well as a flow rate factor, A, dependent on the ice temperature will be considered. Although no substantial implementation-related difficulties are expected, a study of the possible effects on, for example, model stability and computational efficiency and accuracy, is called for. Future efforts will also be devoted to improving the efficiency and scalability of the solvers.

REFERENCES

Bengtsson L (1994) Climate of the 21st century. *Agric. Forest Meteorol.*, **72**(1–2), 3–29

Blatter H (1995) Velocity and stress fields in grounded glaciers: a simple algorithm for including deviatoric stress gradients. *J. Glaciol.*, **41**(138), 333–344

Bochev P and Gunzburger M (2009) *Least-squares finite element methods.* Springer, New York

Cuffey KM and Paterson WSB (2010). *The physics of glaciers*, 4th edn. Butterworth-Heinemann, Oxford

Dukowicz JK, Price SF and Lipscomb WH (2010) Consistent approximations and boundary conditions for ice-sheet dynamics from a principle of least action. *J. Glaciol.*, **56**(197), 480–496

Gagliardini O and Zwinger T (2008) The ISMIP-HOM benchmark experiments performed using the Finite-Element code Elmer. *Cryosphere*, **2**(1), 67–76

Gregory JM and Huybrechts P (2006) Ice-sheet contributions to future sea-level change. *Philos. Trans. R. Soc. London, Ser. A*, **364**(1844), 1709–1731

Hindmarsh RCA (2004) A numerical comparison of approximations to the Stokes equations used in ice sheet and glacier modeling. *J. Geophys. Res.*, **109**(F1), F01012 (10.1029/2003JF000065)

Hutter K (1983) *Theoretical glaciology; material science of ice and the mechanics of glaciers and ice sheets.* D Reidel, Dordrecht

MacAyeal DR (1989) Large-scale ice flow over a viscous basal sediment: theory and application to Ice Stream B, Antarctica. *J. Geophys. Res.*, **94**(B4), 4071–4087

Morland LW (1987) Unconfined ice-shelf flow. In Van der Veen CJ and Oerlemans J eds. *Dynamics of the West Antarctic ice sheet.* D. Reidel, Dordrecht, 99–116

Nye JF (1957) The distribution of stress and velocity in glaciers and ice-sheets. *Proc. R. Soc. London, Ser. A*, **239**(1216), 113–133

Pattyn F (2003) A new three-dimensional higher-order thermo-mechanical ice-sheet model: basic sensitivity, ice stream development, and ice flow across subglacial lakes. *J. Geophys. Res.*, **108**(B8), 2382 (doi: 10.1029/2002JB002329)

Pattyn F and 20 others (2008) Benchmark experiments for higher-order and full-Stokes ice sheet models (ISMIP-HOM). *Cryosphere*, **2**(2), 95–108

Pollard D and DeConto RM (2007) A coupled ice-sheet/ice-shelf/sediment model applied to a marine margin flowline: forced and unforced variations. In Hambrey MJ, Christoffersen P, Glasser NF and Hubbard B eds. *Glacial sedimentary processes and products.* Blackwell, Malden, MA, 37–52

Quarteroni A (2009) *Numerical models for differential problems: modeling, simulation and applications.* Springer-Verlag, Milan

Quarteroni A and Valli A (1994) *Numerical approximation of partial differential equations.* Springer-Verlag, Berlin

Salsa S (2008) *Partial differential equations in action: from modelling to theory.* Springer, Dordrecht

Schoof C and Hindmarsh RCA (2010) Thin-film flows with wall slip: an asymptotic analysis of higher order glacier flow models. *Q. J. Mech. Appl. Math.*, **63**(1), 73–114

APPENDIX. NEWTON'S METHOD

The FO and L1L2 models can be reduced to the solution of a nonlinear equation of the form $\mathcal{F}(u, v) = 0$. In order to find the roots, (u, v), we use Newton's method, which reads:

$$\langle D\mathcal{F}(u^k, v^k), (\delta_u^{k+1}, \delta_v^{k+1}) \rangle = -\mathcal{F}(u^k, v^k), \quad k = 0, 1, \dots ,$$

(A1)

with $\delta_u^{k+1} = u^{k+1} - u^k$ and $\delta_v^{k+1} = v^{k+1} - v^k$. Given an initial guess, (u^0, v^0), one solves Equation (A1) iteratively until $\|\mathcal{F}(u^k, v^k)\|$, in some norm, is less than a given tolerance (other stopping criteria are possible). The expression $\langle D\mathcal{F}(u^k, v^k), (\delta_u^{k+1}, \delta_v^{k+1}) \rangle$ denotes the Gâteaux derivative of $\mathcal{F}$ in the direction $(\delta_u^{k+1}, \delta_v^{k+1})$ evaluated at (u^k, v^k). The Gâteaux derivative is a generalization of the concept of directional derivative. In particular if $\mathcal{F}$ were a vector function from $\mathbb{R}^2$ to $\mathbb{R}^2$, $D\mathcal{F}$ would be the Jacobian matrix in $\mathbb{R}^{2 \times 2}$ and the pairing $\langle \cdot, \cdot \rangle$ would represent the usual matrix vector product. We define the Gâteaux derivative as

$$\left\langle D\mathcal{F}\left(u^k, v^k\right), \left(\delta_u^{k+1}, \delta_v^{k+1}\right) \right\rangle =$$
$$\lim_{h \to 0} \frac{\mathcal{F}\left(u^k + h\,\delta_u^{k+1}, v^k + h\,\delta_v^{k+1}\right) - \mathcal{F}\left(u^k, v^k\right)}{h}.$$

(A2)

In the following we derive the expression of the Gâteaux derivative for the FO and L1L2 models.

Gâteaux derivative for the FO model

Let $\mathcal{F}$ be defined as in Equation (16) (the dependence of $\mathcal{F}$ on (φ_1, φ_2) is understood). A direct computation of the limit in Equation (A2), gives

$$\left\langle D\mathcal{F}\left(u^k, v^k\right), (\delta_u, \delta_v) \right\rangle =$$
$$\begin{bmatrix} \int_\Omega 2(\mu')^k \left(\dot{\boldsymbol{\varepsilon}}_1^k \cdot \nabla\delta_u + \dot{\boldsymbol{\varepsilon}}_2^k \cdot \nabla\delta_v \right) \dot{\boldsymbol{\varepsilon}}_1^k \cdot \nabla\varphi_1 \, d\Omega + \\ \int_\Omega 2\mu^k \dot{\boldsymbol{\varepsilon}}_1(\delta_u, \delta_v) \cdot \nabla\varphi_1 \, d\Omega + \int_{\Gamma_\beta} \beta\delta_u\,\varphi_1 \, ds \\ \int_\Omega 2(\mu')^k \left(\dot{\boldsymbol{\varepsilon}}_1^k \cdot \nabla\delta_u + \dot{\boldsymbol{\varepsilon}}_2^k \cdot \nabla\delta_v \right) \dot{\boldsymbol{\varepsilon}}_2^k \cdot \nabla\varphi_2 \, d\Omega + \\ \int_\Omega 2\mu^k \dot{\boldsymbol{\varepsilon}}_2(\delta_u, \delta_v) \cdot \nabla\varphi_2 \, d\Omega + \int_{\Gamma_\beta} \beta\delta_v\,\varphi_2 \, ds \end{bmatrix},$$

(A3)

where $\dot{\varepsilon}_\lambda^k = \dot{\varepsilon}_\tau(u^k, v^k)$ for $\lambda \in \{1, 2, e\}$, $\mu^k = \mu(\dot{\varepsilon}_e^k)$ and

$$(\mu')^k = \frac{\partial\mu}{\partial(\dot{\varepsilon}_e^2)}\bigg|_{(\dot{\varepsilon}_e = \dot{\varepsilon}_e^k)} = \frac{1-n}{4n} A^{-\frac{1}{n}} (\dot{\varepsilon}_e^k)^{(\frac{1}{n}-3)} = \frac{1-n}{2n} \frac{\mu^k}{(\dot{\varepsilon}_e^k)^2}.$$

(A4)

Gâteaux derivative for the L1L2 model

We consider the L1L2 model, with $\mathcal{F}$ defined as the left-hand side minus the right-hand side of the system of Equation (32),

namely

$$\begin{bmatrix} \int_\Sigma \left(2\bar{\mu}\,\dot{\boldsymbol{\varepsilon}}_{1,b}(u, v) \cdot \nabla_\|\varphi_1 + \beta u\varphi_1 \right) d\Sigma + \int_\Sigma \rho g H \frac{\partial s}{\partial x}\varphi_1 d\Sigma \\ \int_\Sigma \left(2\bar{\mu}\,\dot{\boldsymbol{\varepsilon}}_{2,b}(u, v) \cdot \nabla_\|\varphi_2 + \beta v\varphi_2 \right) d\Sigma + \int_\Sigma \rho g H \frac{\partial s}{\partial y}\varphi_2 d\Sigma \end{bmatrix}.$$

(A5)

A direct computation of the limit in Equation (A2) gives

$$\left\langle D\mathcal{F}(u^k, v^k), (\delta_u, \delta_v) \right\rangle =$$
$$\begin{bmatrix} \int_\Sigma 2(\bar{\mu}')^k \left(\dot{\boldsymbol{\varepsilon}}_{1,b}^k \cdot \nabla_\|\delta_u + \dot{\boldsymbol{\varepsilon}}_{2,b}^k \cdot \nabla_\|\delta_v \right) \dot{\boldsymbol{\varepsilon}}_{1,b}^k \cdot \nabla_\|\varphi_1 \, d\Sigma + \\ \int_\Sigma 2\bar{\mu}^k \dot{\boldsymbol{\varepsilon}}_{1,b}(\delta_u, \delta_v) \cdot \nabla_\|\varphi_1 \, d\Sigma + \int_\Sigma \beta\delta_u\,\varphi_1 \, d\Sigma \\ \int_\Sigma 2(\bar{\mu}')^k \left(\dot{\boldsymbol{\varepsilon}}_{1,b}^k \cdot \nabla_\|\delta_u + \dot{\boldsymbol{\varepsilon}}_{2,b}^k \cdot \nabla_\|\delta_v \right) \dot{\boldsymbol{\varepsilon}}_{2,b}^k \cdot \nabla_\|\varphi_2 \, d\Sigma + \\ \int_\Sigma 2\bar{\mu}^k \dot{\boldsymbol{\varepsilon}}_{2,b}(\delta_u, \delta_v) \cdot \nabla_\|\varphi_2 \, d\Sigma + \int_\Sigma \beta\delta_v\,\varphi_2 \, d\Sigma \end{bmatrix},$$

(A6)

where $\dot{\varepsilon}_b^k = \dot{\varepsilon}_b(u^k, v^k)$, $\tau^k = \tau(u^k, v^k)$, $\mu^k = \mu\left(|\dot{\varepsilon}_b^k|_\|, |\tilde{\tau}|_\perp\right)$ and

$$(\bar{\mu}')^k = \frac{\partial\bar{\mu}}{\partial(|\dot{\varepsilon}_b|_\|^2)}\bigg|_{(\dot{\varepsilon}_b = \dot{\varepsilon}_b^k)} = \frac{1-n}{2A^2} \int_b^s \mu^k \frac{\left(|\tau^k|_\|^2 + |\tilde{\tau}|_\perp^2\right)^{1-n}}{n|\tau^k|_\|^2 + |\tilde{\tau}|_\perp^2} \, dz.$$

(A7)

In the following we detail the calculation of $(\bar{\mu}')^k$. Differentiating both sides of $|\tau^k|_\|^2 = 4(\mu^k)^2 |\dot{\varepsilon}_b|_\|^2$ with respect to $|\dot{\varepsilon}_b|_\|^2$

$$\frac{\partial(|\tau^k|_\|^2)}{\partial(|\dot{\varepsilon}_b|_\|^2)} = 8\mu^k |\dot{\varepsilon}_b|_\|^2 \frac{\partial\mu}{\partial(|\dot{\varepsilon}_b|_\|^2)} + 4(\mu^k)^2,$$

(A8)

and exploiting Equation (22) we have

$$\frac{\partial\mu}{\partial(|\dot{\varepsilon}_b|_\|^2)} = \frac{\mu^k}{2A^2 |\tau^k|_\|^2} \left[A^2 \frac{\partial(|\tau^k|_\|^2)}{\partial(|\dot{\varepsilon}_b|_\|^2)} - \left(|\tau^k|_\|^2 + |\tilde{\tau}|_\perp^2\right)^{1-n} \right].$$

(A9)

In order to have an explicit expression for $\frac{\partial\mu}{\partial(|\dot{\varepsilon}_b|_\|^2)}$ we need to calculate $\frac{\partial(|\tau^k|_\|^2)}{\partial(|\dot{\varepsilon}_b|_\|^2)}$. To this aim we differentiate the squares of both sides of Equation (22) with respect to $|\dot{\varepsilon}_b|_\|^2$:

$$1 = A^2 \left(|\tau^k|_\|^2 + |\tilde{\tau}|_\perp^2\right)^{n-2} \left(n|\tau^k|_\|^2 + |\tilde{\tau}|_\perp^2\right) \frac{\partial(|\tau^k|_\|^2)}{\partial(|\dot{\varepsilon}_b|_\|^2)}.$$

(A10)

Combining Equations (A9) and (A10) we get

$$\frac{\partial\mu}{\partial(|\dot{\varepsilon}_b|_\|^2)} = \frac{1-n}{2A^2} \mu^k \frac{\left(|\tau^k|_\|^2 + |\tilde{\tau}|_\perp^2\right)^{1-n}}{n|\tau^k|_\|^2 + |\tilde{\tau}|_\perp^2}.$$

(A11)

The result, Equation (A7), follows straightforwardly since $\dot{\varepsilon}_b$ does not depend on z.